Ground-Effect-Aware Modeling and Control for Multicopters

Tiankai Yang[1,2], Kaixin Chai[2], Jialin Ji[1,2], Chao Xu[1,2], and Fei Gao[1,2]

***Abstract*—The ground effect on multicopters introduces several challenges, such as control errors caused by additional lift, oscillations that may occur during near-ground flight due to external torques, and the influence of ground airflow on models such as the rotor drag and the mixing matrix. This article collects and analyzes the dynamics data of near-ground multicopter flight through various methods, including fluid simulation, force measurement brackets, and real-world flights. For the first time, we summarize the mathematical model of the external torque of multicopters under ground effect. The influence of ground airflow on rotor drag and the mixing matrix is also verified through adequate experimentation and analysis. Through simplification and derivation, the differential flatness of the multicopter's dynamic model under ground effect is confirmed. To mitigate the influence of these disturbance models on control, we propose a control method that combines dynamic inverse and disturbance models, ensuring consistent control effectiveness at both high and low altitudes.**

***Index Terms*—Ground effect, multicopter control, aerodynamic analysis, fluid simulation, disturbance modeling.**

I. Introduction

Thanks to the simple mechanical design and high maneuverability, multicopters are widely used in both open sky and indoor environments. However, near-ground operations are unavoidable in many applications. For example, using a multicopter with an arm to grab an object close to the ground [1], [2], planning a near-ground trajectory to use the extra thrust provided by ground effect to save energy [3], flying in the tunnel [4] or along the wall [5] automatically landing on the surface of the object [6], [7], and so on. In these scenarios, when approaching rigid structures, multicopters are disturbed by the airflow near surfaces of ground or objects, which significantly influences the safety and stability.

This phenomenon, usually known as *ground effect*, has been extensively analyzed by researchers [8]–[11]. Most works focus on precisely modeling the extra lift produced by ground effect, typically with a height-dependent external force function. In this way, a feed-forward control signal can be calculated using the model, and is then applied to cancel the disturbance while the multicopter flying with a static height and attitude. However, the disturbances imposed on multicopters by ground effect go beyond this.

The first one is the external torque. When a multicopter flies near flat ground and its attitude is not horizontal, the propellers closer to the ground generate more thrust, creating a torque that tends to level the multicopter's attitude [9]. We call it the *leveling torque*. This could result in oscillations or a decrease in control precision.

Corresponding author: Fei Gao, Chao Xu
[1]Institute of Cyber-Systems and Control, College of Control Science and Engineering, Zhejiang University, Hangzhou 310027, China.
[2]Huzhou Institute, Zhejiang University, Huzhou 313000, China.
E-mail: tkyang@zju.edu.cn kaixinchai@outlook.com fgaoaa@zju.edu.cn

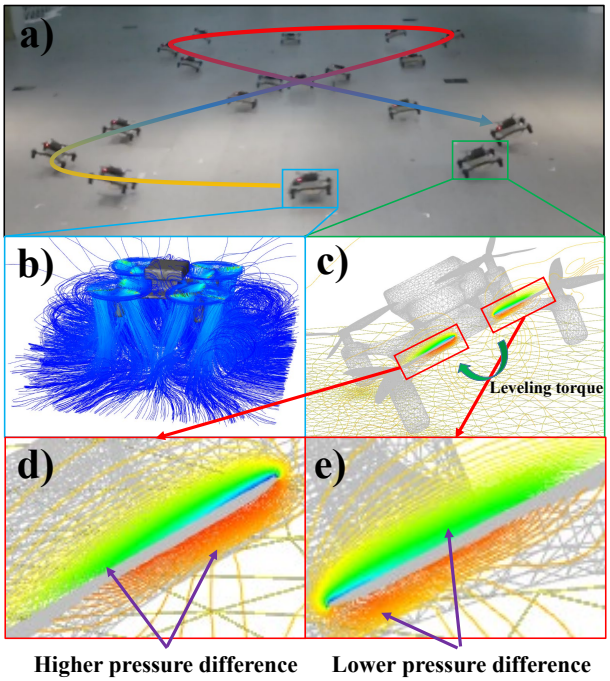

Fig. 1: (a) The quadrotor is flying close to the ground, ensuring a small distance from the ground surface. (b) The airflow around a quadrotor flying near the ground. The change in the direction of the airflow results in additional lift. (c) Air pressure around the rotors of a tilted quadrotor near the ground (red for high pressure, green for low pressure). (d)(e) The closer the rotor is to the ground, the greater the pressure difference between the upper and lower surfaces, resulting in a torque that tends to level the quadrotor.

The second one is the decrease in rotor drag. A blade on a rotating propeller experiences lift from the air and resistance applied to the plane of rotation. This resistance is usually proportional to the rotor speed and the forward flight speed [12]. Since the total thrust during high-altitude flight is maintained near the hover throttle, the rotor drag coefficient is commonly modeled as a constant [13], [14]. However, as mentioned earlier, the multicopter needs a lower throttle when flying near the ground, so it can be inferred that the rotor drag also decreases. The actual situation may be more complicated due to the presence of near-ground airflow. We will verify whether the rotor drag decreases as expected in the following experiments.

The third one is not usually considered is the escape of the lift airflow when flying at high speed near the ground. Kan et al. [15] analyze the variations in additional thrust during forward flight near the ground. When hovering, the airflow

bouncing off the ground surface creates a high-pressure layer, resulting in an additional thrust for the multicopter. During high-speed forward flight, some near-ground airflow escapes, leading to a reduction in the additional thrust.

These problems make it difficult for multicopters to maintain a tilted attitude near the ground in order to generate horizontal acceleration. As a result, the existing methods are only suitable for situations such as taking off, landing and near-ground hovering, posing difficulties in tracking a trajectory close to the ground. Therefore, exploring the dynamics model of the multicopter under the ground effect is necessary.

For this purpose, we establish both simulated and real-world force and torque measurement platforms (Sec. IV). Real-flight experiments are conducted to collect external disturbance data in various scenarios. Based on the collected data, we develop an external torque model (Sec. V-B) for ground effect (first-time) and validate the impact of ground effect on rotor drag (Sec. V-D) and mixing matrix (Sec. V-C). We simplify the drag and thrust models and convert the torque model to the payload model (Sec. VI-A). These simplifications and equivalences make the dynamic model of a multicopter differential flat (Sec. VI) under the influence of ground effects, which allows to generate feedforward control commands based on the trajectory. We combine the model-based control method (Sec. VII) with the model-free method to effectively improve the control precision (Sec. VIII).

This paper has the following contributions:

- A series of methods (including simulation, force measuring bracket and real flight) are used to collect complete dynamic data of multicopters under ground effect.
- For the first time, propose a model for the leveling torque. Validate other models under ground effect including rotor drag and mixing matrix.
- Simplify the dynamic model of the multicopter under ground effect to maintain differential flatness, and design a control method that takes both ground effect model and unknown disturbances into account.

II. Related Work

A. Additional Thrust under Ground Effect

The study of the ground effect of the blades is initially carried out on helicopters [16]. The influence of the helicopter's body shape on the parameters of the ground effect is mainly reflected in the radius of the propeller and the distance between the blade plane and the ground. Other influencing factors include air density, rotor speed, blade pitch angle and the incoming flow speed in the direction of the rotation axis.

Since the helicopter has only one rotor, its dynamic model is relatively simple compared to the multicopter. For a multicopter, an air convection area is formed under the entire body, and its ground effect is greater than the superposition of individual rotors. Therefore some ground effect models [9], [10], [15] are proposed to adapt to the multicopter. Sanchez-Cuevas's work [9] introduced some correction terms from the helicopter' ground-effect model to the multicopter, making it possible to obtain the model without identifying a series of polynomial coefficients.

B. The Neglected Leveling Torque Model

The main focus of this article is to model and compensate for the leveling torque. There are two common solutions in previous works.

The first solution is inner loop tuning. At a certain height, when the multicopter tilts more, it experiences a stronger leveling torque from the ground effect, which can be considered linear at a small angle. Since the leveling torque is aiming to level the multicopter's attitude, the relationship is equivalent to fixing a payload under the multicopter (described in detail in Sec. VI-A). Furthermore, it can be equivalent to shifting the center of gravity down and increasing the moment of inertia, which can be handled by adjusting the gain of the attitude and angular velocity loops. Since the intensity of the ground effect varies at different altitudes, there should be a set of suitable parameters at each altitude. But the lack of models makes tuning parameters a trouble. However, the researchers who use inner loop tuning do not realize that they are compensating the torque by doing so.

For example, Sanchez et al. [9] believe that the leveling torque is not significant enough and only makes the multicopter more stable, so it is not modeled or considered in their control framework. Their work focuses on the additional thrust generated by ground effect on certain propellers when the multicopter passes over an obstacle, resulting in a torque (*obstacle torque*) pushing the multicopter away from the obstacle. In the experiment, a table is placed under the path of the horizontal flight of the multicopter, which means there are actually only two altitudes during the flight: the *constant* and *infinite*. Using the *obstacle torque* model as feedforward, he introduced a bias of the attitude command, and the final output command is the desired attitude of the multicopter. To solve the leveling torque problem, the attitude controller parameters of flight control only need to be adjusted according to the specific height of this scene, and do not need to be adapted to all heights.

Another example is Neural Landing [17], where Shi et al. design a network based on dynamics and state information of multicopters to predict external forces near the ground. They do not think the leveling torque is significant enough to be compensated for. But the parameters in their controller framework, such as the error gain of angular velocity, can mitigate the oscillations caused by the leveling torque. But the parameters in its controller frame, such as the angular velocity error gain, can mitigate the oscillations caused by horizontal torques Adjusting parameters according to the low-altitude scenario will reduce the control accuracy at high attitude. Still, it does not affect landing and low altitude flights.

The second solution is a disturbance observer. The leveling torque can be obtained by an observer [10], [18] and then compensated (incremental compensation [19], [20] is also possible). Such methods are not effective enough. They believe that the external torque in the next time period is about equal to the one observed in the previous time period. It is effective for some slowly changing external disturbances, such as the gravity torque caused by the shift of the center of gravity on the *XOY plane* of the body coordinate system. Because even if

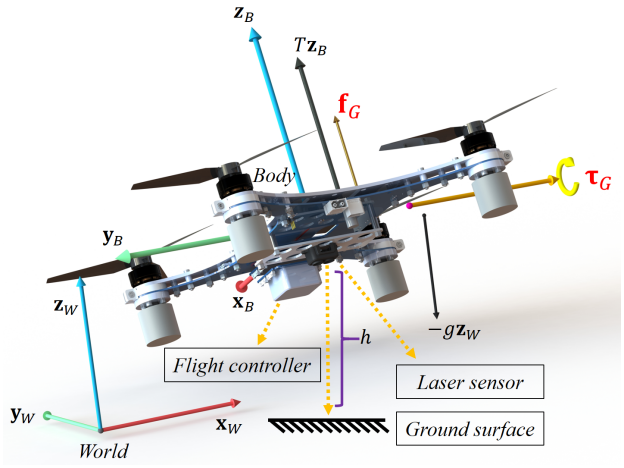

Fig. 2: The coordinate systems of the multicopter.

the multicopter has a certain attitude tilt, the lever arm of the gravity torque basically remains unchanged. For other cases, such as the shift of the center of gravity in the *Z axis* of the body coordinate system or the ground effect, the external torque is proportional to the tilt angle and changes at high frequency, resulting in a delay in the disturbance estimation, and the torque compensation cannot eliminate the oscillations.

C. Rotor Drag

The previous work [12], [21] provide a detailed explanation of the causes of rotor drag, which is related to the relative speed between the rotor and the air. When hovering, the relative air velocity is proportional to the rotor speed. During forward flight, the blades moving forward have a higher relative air velocity than those moving backward. This causes the blade to experience different resistance at different phases, and the resultant force of the resistance received by the whole propeller is not zero . The rotor drag is proportional to the total thrust because the difference in the relative air velocity of the blades in different phases is proportional to the propeller speed.

III. Basic Symbol Representation

Some coordinate systems, forces, and torques in this work are shown in Fig. 2. We use

$$[\boldsymbol{x}_W, \boldsymbol{y}_W, \boldsymbol{z}_W] = \boldsymbol{I}_3 \tag{1}$$

to represent the 3 orthonormal bases of the *world coordinate system*. $\boldsymbol{I}_3$ is the identity matrix. The orientation of the multicopter is denoted by

$$\boldsymbol{R} = [\boldsymbol{x}_B, \boldsymbol{y}_B, \boldsymbol{z}_B], \tag{2}$$

where $\{\boldsymbol{x}_B, \boldsymbol{y}_B, \boldsymbol{z}_B\}$ are a set of orthogonal bases of the *body coordinate system* of the multicopter.

The position of the multicopter's geometric center in the *world coordinate system* is $\boldsymbol{p}$, and $\{\boldsymbol{v}, \boldsymbol{a}, \boldsymbol{j}\}$ are the velocity, acceleration and jerk of the multicopter in the *world coordinate system* respectively.

The Euler angles of the multicopter in the *world coordinate system* are expressed in the order of $Z-Y-X$ rotation as $\boldsymbol{\xi} = \{\varphi, \gamma, \phi\}$. The rotation matrix around an axis of $Z-Y-X$ can be expressed as $T_Z(\varphi)$, $T_Y(\gamma)$ and $T_X(\phi)$ respectively. The angular velocity and angular acceleration of the multicopter in the *body coordinate system* are expressed as $\boldsymbol{\omega}$ and $\boldsymbol{\beta}$.

The dynamics model of the multicopter can be written in the following form:

$$\begin{aligned} m\boldsymbol{a} &= -g\boldsymbol{z}_W + T\boldsymbol{z}_B + \boldsymbol{f}_G + \boldsymbol{f}_D \\ \boldsymbol{J}\dot{\boldsymbol{\omega}} &= -\boldsymbol{\omega} \times \boldsymbol{J}\boldsymbol{\omega} + \boldsymbol{\tau}_B + \boldsymbol{\tau}_G + \boldsymbol{\tau}_{ext}, \end{aligned} \tag{3}$$

where m and $\boldsymbol{J}$ are the mass and the inertia tensor of the multicopter respectively, $\boldsymbol{g}$ is the acceleration of gravity.

The forces and torques in the dynamic model are as follows:

Symbol	Description
$T\boldsymbol{z}_B$	Thrust generated by the rotors
$\boldsymbol{f}_G$	Additional force generated by ground effect
$\boldsymbol{\tau}_B$	Torque generated by the rotors
$\boldsymbol{f}_D$	Rotor drag
$\boldsymbol{\tau}_G$	Leveling torque generated by ground effect
$\boldsymbol{\tau}_{ext}$	The sum of unmodeled external torques

For a quadrotor, the total thrust and torque in the body coordinate system generated by all the rotors can be expressed as (4):

$$\begin{bmatrix} T \\ \boldsymbol{\tau}_B \end{bmatrix} = \boldsymbol{M}\boldsymbol{N}^2 = diag\left(k_T, \frac{\sqrt{2}b}{4}k_{TX}, \frac{\sqrt{2}b}{4}k_{TY}, k_I\right) \begin{bmatrix} 1 & 1 & 1 & 1 \\ -1 & 1 & 1 & -1 \\ -1 & 1 & -1 & 1 \\ -1 & -1 & 1 & 1 \end{bmatrix} \begin{bmatrix} {n_1}^2 \\ {n_2}^2 \\ {n_3}^2 \\ {n_4}^2 \end{bmatrix}. \tag{4}$$

b represents the distance between the diagonal rotors. n_i represents the rotation speed of each rotor. k_T is the thrust coefficient. k_{TX} and k_{TY} are the torque coefficients in the roll and pitch directions, respectively. k_I is the inverse torque coefficient of the rotors. $\boldsymbol{M}$ is the mixing matirx of the quadrotor. n_i is the rotor speed (unit: rotation-per-minute, rpm), $\boldsymbol{N}^2$ is a 4×1 matrix consisting of the square of the rotor speeds.

The mechanical frame of the quadrotor is not completely centrosymmetry, and the body obstructs the airflow of the rotor, therefore it can be assumed:

$$k_T \neq k_{TX} \neq k_{TY}. \tag{5}$$

In the next section, We will introduce how to explore the models of the various external disturbances mentioned above using experimental or simulation methods.

IV. Methods for Exploring and Validating Models

In this section, we will introduce how to set up the environments to collect and analyze the dynamic data of multicopters under ground effect. The environments include the single-rotor platfrom (Fig. 3a), the quadcopter platform (Fig. 3(b)(c)), fluid simulation(Fig. 3(d)(e)), etc. Additionally, we introduce the *Spearman correlation coefficient* [22] to ascertain the specific factors related to external disturbances.

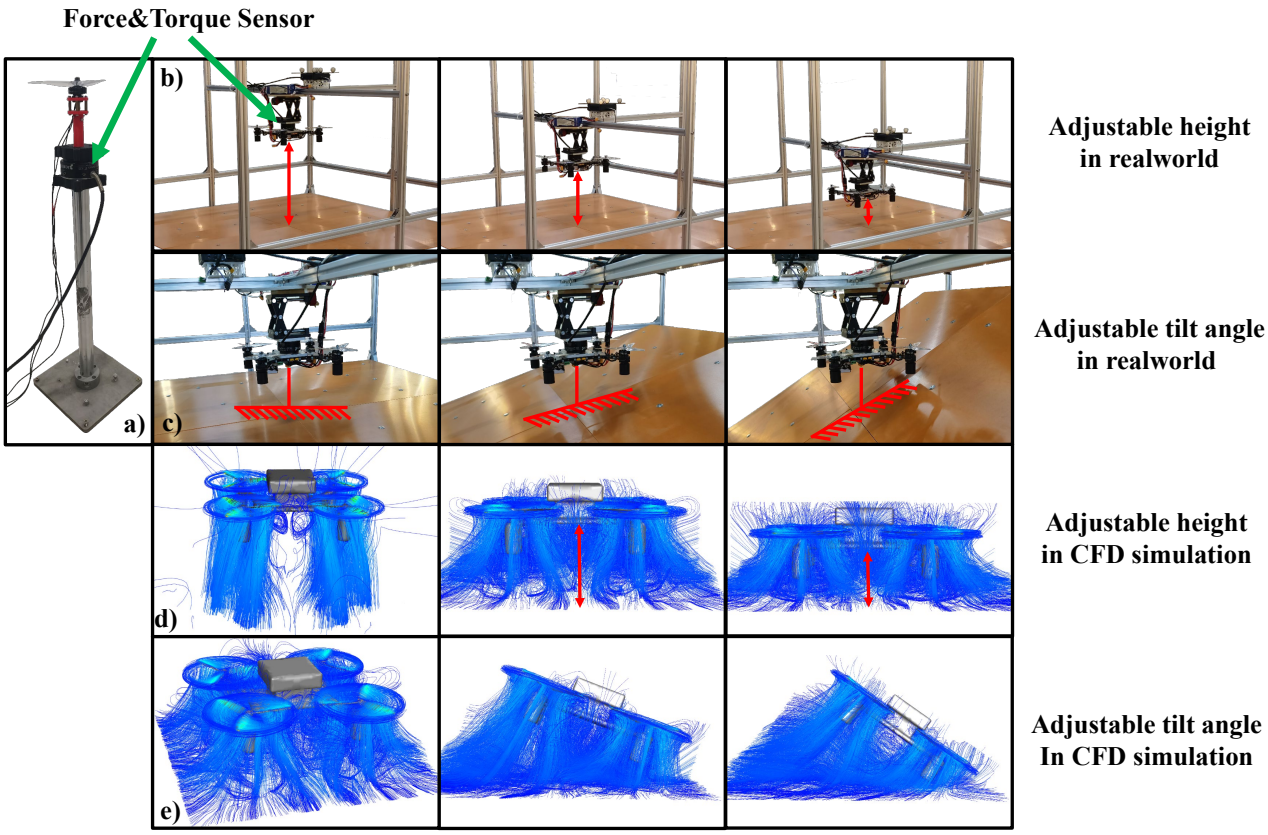

Fig. 3: Experimental environment for model validation (including both real-world and simulation). **(a)** Test platform for an individual rotor. **(b)(c)** The aluminum profile frame platform for the quadrotor in the real world. The tilt angle of the ground surface can be adjusted to simulate the tilt angle of the quadrotor. **(d)(e)** Simulation environment for the quadrotor under ground effect.

A. Dynamic Measurement Platform in real-world

We set up dynamics testing platforms for a single rotor and a quadrotor separately. Both of them are equipped with a six-axis force and torque sensor.

1) The single-rotor platform: The platform (Fig. 3a) is fixed on the ground, which can measure the rotor speed, thrust, and torque of a single motor when it rotates. The rotor is positioned far away from the ground to minimize ground effect. Some connecting mechanisms use soft 3D-printed parts (TPU material), effectively reducing the noise in sensor data caused by rotor rotation.

2) The quadrotor platform: In the platform illustrated in Fig. 3(b)(c), the entire quadrotor is fixed on the aluminum profile frame. A force and torque sensor is fixed between the frame and the quadrotor. A resin board ($1.2m \times 1.2m$) is placed under the quadrotor to simulate the ground. A series of mechanical structures are available for adjusting the tilt angle of the board and the height of the quadrotor. This setup allows for simulating quadrotor flights near the ground with a forward tilt angle. An array laser sensor is used to measure the distance between the ground board and the quadrotor. The tilt angle of the ground is determined by an electronic inclinometer.

It's worth noting that we adjust the angle of the ground board rather than the angle of the quadrotor. In other words, we simulate the quadrotor tilting by tilting the ground board while keeping the quadrotor level. This is because if the quadrotor tilts, it will generate a gravity moment associated with the tilt angle. Additionally, when the rotors rotate, there will be a torque related to the rotor speed since the sensor center does not coincide with the thrust line of the rotors. Both of these factors would interfere with the measurement of the torques generated by ground effect.

B. Dynamic Measurement Environment in Simulation

In this paper, we aim to propose an accurate model for ground effects, with the ultimate goal of improving the control stability of multicopters in proximity to the ground. This necessitates the acquisition of extensive experimental data to facilitate both the development and validation of the proposed model. To this end, we employ the aerodynamics simulation tool ANSYS to automate extensive data collection. The following outlines our setups.

Firstly, to ensure the simulation data accurately supports model development and validation, it must closely mirror real-world conditions [23]. We create a precise 3D quadrotor model (Fig. 4(a)), paying special attention to the propeller—a

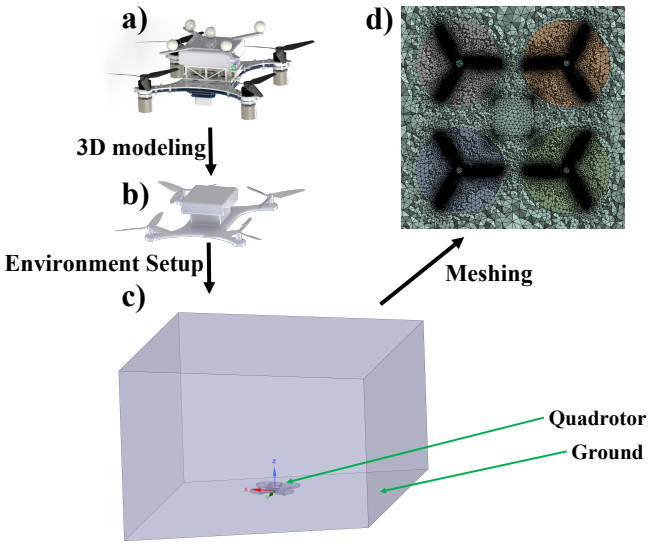

Fig. 4: Setup for the fluid simulation.

key component in quadrotor flight, responsible for generating thrust and torque through its interaction with air [12]. We use 3D laser scanning to capture an accurate model of the propeller (Fig. 4(b)). However, it's important to note that, unlike actual conditions where propellers can deform at high speeds, our simulations assume propellers are rigid. Despite this simplification, our findings show that the trends in simulation closely align with real-life experiments.

Secondly, The accuracy of fluid dynamics simulations greatly depends on the quality and setup of the mesh [24]. We import our quadrotor model into a meshing tool to divide the space into manageable sections. To efficiently simulate various conditions without overly lengthy computation times, we balance the accuracy and computational speed. Firstly, we employ a combination of coarse and fine meshes [25]: coarse tetrahedral meshes for the larger fluid domain to enhance computational efficiency, and finer meshes with inflation layers (Fig. 4(d)) around the propeller surfaces to guarantee precision. Secondly, through a mesh independence study [26], we identified the coarsest mesh that could still deliver acceptable accuracy. This strategy significantly reduces computation times without substantially compromising the accuracy of our simulations.

Thirdly, in our simulations, we chose the $k-\epsilon$ turbulence model [27], which is particularly well-suited for scenarios where air can be assumed as an incompressible fluid. This assumption aligns with our quadrotor's aerodynamic conditions near the ground. For solving the equations, we opted for double-precision arithmetic to ensure high accuracy in our calculations. The SIMPLE algorithm [28] is used for pressure-velocity coupling, enhancing the stability and convergence of our simulations. Moreover, we apply second-order upwind discretization to the momentum equations, improving the accuracy of our aerodynamic force and torque predictions. These settings in ANSYS allow us to achieve reliable and detailed insights into the aerodynamic behavior of a quadrotor across a range of altitudes, angles, and propeller speeds. Our goal through this meticulous simulation setup was to gather comprehensive data on the aerodynamic forces and moments that impact the quadrotor near the ground, ensuring our model's development and validation are based on robust and precise computational findings.

C. Additional Methods

1) Real-world flight: In addition to using the dynamic measurement platform and the simulation environment, we also conduct real-world flight experiments to collect disturbance data experienced by the quadrotor during near-ground flights.

We introduce the following external force and torque observer:

$$\begin{aligned}\tilde{\boldsymbol{a}}_{ext} &= (\boldsymbol{a}-\boldsymbol{g})_f^{imu} - \boldsymbol{z}_B T_f/m \\ \tilde{\boldsymbol{\tau}}_{ext} &= \boldsymbol{J}\dot{\boldsymbol{\omega}}_f + \boldsymbol{\omega}_f \times \boldsymbol{J}\boldsymbol{\omega}_f - \boldsymbol{\tau}_B.\end{aligned} \tag{6}$$

The subscript $(\cdot)_f$ indicates that the data has been filtered through a low-pass filter. $(\boldsymbol{a}-\boldsymbol{g})^{imu}$ is the raw acceleration data captured by the Inertial Measurement Unit (IMU),

2) Mechanical model: We can directly determine the inertia moment and the center of gravity of the quadrotor with the Mechanical model. Since the total mass of the Mechanical model is nearly equal to the actual total mass, it can be assumed that the calculated inertia moment from the Mechanical model is also nearly equal to the actual one. In addition to being used for model exploration and validation, the controller also directly calls these parameters in practice.

3) Correlation coefficient: To explore and validate the relationship between external disturbances introduced by ground effect and various variables (height, rotor speed, tilt angle, etc), we calculate the *Spearman's rank correlation coefficient* [22]. This statistical tool assesses the existence and strength of monotonic relationships between nonlinear parameters.

For two datasets, x_i and y_i, of the same size n, both sets are ranked as $R(x_i)$ and $R(y_i)$. The Spearman's rank correlation coefficient r_s can be computed:

$$r_s(x,y) = \frac{\operatorname{cov}[R(x), R(y)]}{\sigma[R(x)]\,\sigma[R(y)]}. \tag{7}$$

$\operatorname{cov}[R(x), R(y)]$ represents the covariance of the ranked variables, while $\sigma[R(x)]$ and $\sigma[R(y)]$ signify their respective standard deviations.

The variables we focus on are height, tilt angle, and rotor speed. When exploring the correlation between external disturbances and rotor speeds, it is difficult to establish a direct connection between the speed of individual rotors and the overall dynamics of the quadrotor. Consequently, the rotor speeds are transformed into $\boldsymbol{N}_{base}$:

$$\boldsymbol{N}_{base} = \operatorname{diag}(k_T, k_{TX}, k_{TY}, k_I)^{-1}\boldsymbol{M}\boldsymbol{N}^2. \tag{8}$$

In data analysis, $\boldsymbol{N}_{base}(1)$ represents the composite rotor speeds corresponding to total thrust T, while $\boldsymbol{N}_{base}(2)$, $\boldsymbol{N}_{base}(3)$, and $\boldsymbol{N}_{base}(4)$ represent the composite rotor speeds corresponding to roll, pitch, and yaw torque (${\boldsymbol{x}_W}^\top\boldsymbol{\tau}_B$, ${\boldsymbol{y}_W}^\top\boldsymbol{\tau}_B$, ${\boldsymbol{z}_W}^\top\boldsymbol{\tau}_B$), respectively.

Spearman's rank correlation coefficient between disturbances and variables are shown in TABLE. I. The results of parameter identification are shown in TABLE. II. Relevant experiments are described in Sec. V.

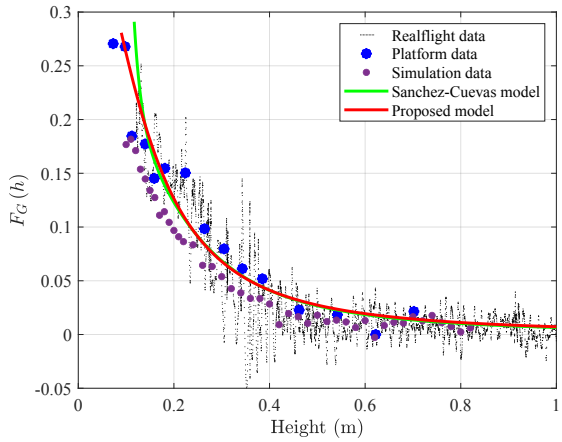

Fig. 5: Data and model of the additional thrust $\boldsymbol{f}_G$.

V. Models under Ground effect

A. Thrust Model under Ground effect

1) Model: The total thrust generated by the rotors can be expressed as:

$$T = \sum_{i=1}^{4} k_T {n_i}^2. \tag{9}$$

The additional force generated by ground effect can be expressed as:

$$\boldsymbol{f_G} = F_G(h)\, T \boldsymbol{z}_B. \tag{10}$$

$F_G(h)$ is a function related to the distance h from the ground to the center of the rotor plane:

$$F_G(h) = \frac{g_2}{h^2 + g_1}, \tag{11}$$

where g_1 and g_2 are constants.

In previous studies [9], [10], [15], various forms of the function $F_G(h)$ have been employed. We choose the above form (11) primarily because of its simplicity, fewer parameters, and most importantly, its derivative form can explain the model of the leveling torque (18) by ground effect, which is proposed in Sec. V-B.

2) Experiment: We conduct a series of experiments to verify the model of the additional thrust model under ground effect and identify the relevant parameters.

During the quadrotor platform experiment, we align the ground board horizontally, as illustrated in Fig. 3(b). We adjust the distance between the ground board and the quadrotor, collecting essential data including rotor speed and height above the ground. The $F_G(h)$ function is measured using the following formula:

$$\tilde{F}_G(h) = \frac{{\boldsymbol{z}_W}^\top \tilde{\boldsymbol{f}}}{\tilde{T}} - 1. \tag{12}$$

$\tilde{\boldsymbol{f}}$ is the measurement of the force sensor. $\tilde{T}$ is the measurement of (9).

This method also applies to the data we collect in the CFD simulation.

During the real-world flight experiment, the quadrotor gradually reduces its hover altitude, and the relevant data (IMU and rotor speed) is collected for estimating the $F_G(h)$ function:

$$\tilde{F}_G(h) = \frac{m{\boldsymbol{z}_W}^\top \tilde{\boldsymbol{a}}_{ext}}{\tilde{T}}, \tag{13}$$

where $\tilde{\boldsymbol{a}}_{ext}$ is the external force obtained by (6).

Subsequently, the data are shown in Fig. 5. Our model in (11) matches the data from the platform experiment, CFD simulation and the flight experiment. It is generally consistent with Sanchez's model [9]. The associated parameters can be identified and are presented in TABLE. II.

To prove that $\boldsymbol{f}_G$ remains unaffected by the tilt angle of the quadrotor and is oriented in the z-axis of the quadrotor body coordinate system, we gradually adjuste the tilt angle and height of the ground board as illustrated in Fig. 3(b)(c) and collect relevant data.. Correlation coefficients between $\boldsymbol{f}_G$ and various variables are computed, as detailed in TABLE. I. The result, $r_s\left[\boldsymbol{f}_G, \boldsymbol{N}_{base}(1)\right] = 0.0054$, indicates a lack of correlation between $\boldsymbol{f}_G$ and the tilt angle δ.

B. The Leveling Torque Generated by Ground Effect

During low-altitude flight, the quadrotor's tilt angle relative to the ground leads to varying ground effects on its rotors. Rotors closer to the ground experience a more significant additional thrust, creating an external leveling torque ($\boldsymbol{\tau}_G$) that tends to level the quadrotor's attitude.

1) Model assumptions: We can make some reasonable assumptions about the model of leveling torque:

- $\boldsymbol{\tau}_G$ and δ: As the tilt angle increases, the difference in distance between the diagonal rotors and the ground increases, resulting in a larger thrust difference and an increase in leveling torque.
- $\boldsymbol{\tau}_G$ and T: As the total thrust increases, the additional thrust from ground effect also increases. This results in a proportional increase in thrust difference between higher and lower rotors, leading to an increase in leveling torque.
- $\boldsymbol{\tau}_G$ and h: If the absolute value of the derivative of the additional thrust function $\dot{F}_G(h)$ is large at a certain height, it means that near that height, rotors at different heights will produce a larger thrust difference, resulting in a larger leveling torque.

2) Explore some rules through simulation: The assumptions about the relationship between thrust, tilt angle, and leveling torque is relatively straightforward to ubderstand. However, there may be differing viewpoints on the relationship between leveling torque and altitude. For instance, some may assume that the closer the height to the ground, the stronger the ground airflow, leading to greater leveling torque. Therefore, we attempt to validate this through fluid simulation (Sec. IV-B).

During the simulation, we keep the quadrotor's tilt angle and rotor speed constant while adjusting its height from the

TABLE I: Spearman's rank correlation coefficient between variables.

$r_s(\cdot,\cdot)$	${\boldsymbol{x}_W}^\top \boldsymbol{\tau}_B$	${\boldsymbol{z}_W}^\top \boldsymbol{\tau}_B$	${\boldsymbol{y}_W}^\top \boldsymbol{\tau}_G$	${\boldsymbol{y}_W}^\top \boldsymbol{\tau}_G / \sin\delta$	$\boldsymbol{f_G}$
$\boldsymbol{N}_{base}(1)$	-	-	$\uparrow -0.6640^{\text{V-B}}$	-	$\uparrow +0.4703^{\text{V-A}}$
$\boldsymbol{N}_{base}(2)$	$\uparrow +0.8245^{\text{V-C}}$	-	-	-	-
$\boldsymbol{N}_{base}(3)$	-	-	-	-	-
$\boldsymbol{N}_{base}(4)$	-	$\uparrow +0.9251^{\text{V-C}}$	-	-	-
h	$\downarrow +0.0284^{\text{V-C}}$	$\downarrow +0.1781^{\text{V-C}}$	$\uparrow +0.3384^{\text{V-B}}$	-	$\uparrow -0.5465^{\text{V-A}}$
δ	-	-	-	$\downarrow +0.0930^{\text{V-B}}$	$\downarrow +0.0054^{\text{V-A}}$

TABLE II: Model parameters.

Symbol	Value	Name	Method
k_T	$4.0083\times10^{-8}\text{N/rpm}^2$ $3.7840\times10^{-8}\text{N/rpm}^2$ $4.2958\times10^{-8}\text{N/rpm}^2$ $3.1915\times10^{-8}\text{N/rpm}^2$	Thrust coefficient	Single-rotor platform Quadrotor platform Real flight by hovering Simulation
k_{TX} k_{TY}	$4.678\times10^{-8}\text{N/rpm}^2$ $3.588\times10^{-8}\text{N/rpm}^2$	Torque by thrust coefficient (roll) Torque by thrust coefficient (pitch)	Quadrotor platform
k_I	$6.3859\times10^{-10}\,(\text{N}\cdot\text{m})/\text{rpm}^2$	Rotor torque coefficient	Single-rotor platform
J_R	$1.0556\times10^{-4}\text{kg/m}^2$	Rotor inertia	Single-rotor platform
g_1 g_2 g_3 g_4 g_5	1.804×10^{-2} 7.339×10^{-3} -3.365×10^{-1} 4.126×10^{-2} 6.494×10^{-2}	Ground effect coefficient	Quadrotor platform
c_2 c_1 c_0	-1.448471×10^{8} 5.228928×10^{8} 1.033111×10^{8}	Throttle curve parameter	Quadrotor platform
d_x d_y	$0.3970\text{N}/(\text{m/s})$ $0.3300\text{N}/(\text{m/s})$	Rotor drag coefficient	Real flight
m	1.696kg 1.562kg	Mass of the quadrotor	Electronic scale Mechanical model
I_x I_y I_z	0.00745220kg/m^2 0.00792752kg/m^2 0.01249522kg/m^2	Inertia of the quadrotor	Mechanical model

ground. The data on leveling torque is illustrated in Fig. 6. It can be observed that the trend of leveling torque variation with height aligns with the trend of the derivative of (11).

3) Possible mathematical explanations: We will try to conduct some mathematical derivations to explain these assumptions and simulation results.

Assuming the additional force $\boldsymbol{\tau}_G$ by ground effect is distributed on a circle with the quadrotor's center as its center and the diagonal wheelbase b as its diameter. The center of this circle is located at a height h above the ground, and the height of the points on the circle is $H(\theta)\{\theta\in[0,2\pi)\}$. The point closest to the ground corresponds to θ=0. $D(\theta)$ represents the distribution density function of the ground effect force $\boldsymbol{\tau_G}$ on the circle. The relationship can be expressed as follows:

$$\begin{aligned}
&\int_0^{2\pi} D(\theta)\,d\theta = F_G(h)\,T\\
&D(\theta) = F_G[H(\theta)]\,T/2\pi\\
&H(\theta) = h - \frac{b}{2}\sin\delta\cos\theta,
\end{aligned} \tag{14}$$

where δ is the angle between the Z-axis of the body system and the world coordinate system.

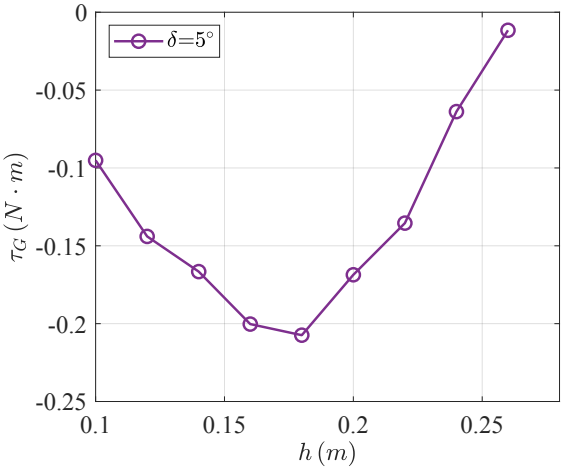

Fig. 6: The leveling torque in simulation.

We assume that around a certain height, $\dot{F}_G(h)$ is a constant

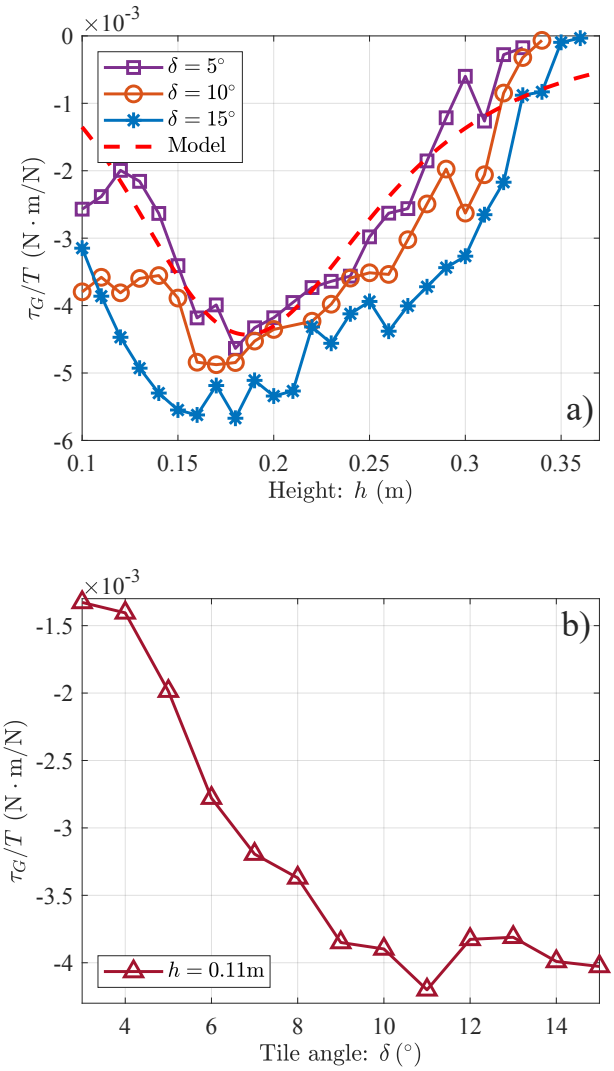

Fig. 7: Leveling torque measured on the quadrotor platform.

value:

$$F_G\left[H\left(\theta\right)\right] = F_G\left(h\right) - \frac{b}{2}\sin\delta\cos\theta\dot{F}_G\left(h\right). \tag{15}$$

The torque $|\boldsymbol{\tau}_G|$ is created by the $|\boldsymbol{f}_G|$ distributed on the circle:

$$\begin{aligned}|\boldsymbol{\tau}_G| &= \int_0^{2\pi} D\left(\theta\right)\frac{b}{2}\cos\theta d\theta \\ &= \frac{bT}{2\pi}\int_0^{\pi}\left[F_G\left(h\right) - \frac{b}{2}\sin\delta\cos\theta\dot{F}_G\left(h\right)\right]\cos\theta d\theta \\ &= -\frac{1}{8}b^2\sin\delta\dot{F}_G\left(h\right)T.\end{aligned} \tag{16}$$

The vector form of $\boldsymbol{\tau}_G$ in the body coordinate system can be written as

$$\mathbf{R}\tau_G = |\tau_G|\left(\mathbf{z}_B \times \mathbf{z}_W\right) = M_G\left(h\right)T\left(\mathbf{z}_B \times \mathbf{z}_W\right). \tag{17}$$

$M_G\left(h\right)$ can be regarded as

$$M_G\left(h\right) = \frac{g_5 h}{\left(h^2 + g_3 h + g_4\right)^2}. \tag{18}$$

4) Calibrate parameters with the real-world platform: We need to validate the above model and calibrate parameters through real-world experiments.

As shown in Fig. 3(b)(c), on the quadrotor platform, we adjust the tilt angle of the ground board and the height of the quadrotor, increase throttle and maintain consistent speeds for all four rotors. Data on tilt angle, height, rotor speeds, and torques are collected. From TABLE. I, it is evident that $\boldsymbol{\tau}_G$ exhibits a strong correlation with both altitude h, tilt angle, and average rotor speed.

- $\boldsymbol{\tau}_G$ and T
  Fig. 8 illustrates the relationship between leveling torque $\boldsymbol{\tau}_G$ and average rotational speed $\|n_i\|$ under varying tilt angles and heights on the quadrotor platform. It is evident that, under different tilt angles and heights, there is always a proportional relationship between the leveling torque and the square of the average rotation speed (or thrust according to (9)):

$$|\boldsymbol{\tau}_G| \sim \|n_i\|^2 \sim T. \tag{19}$$

- $\boldsymbol{\tau}_G$ and δ
  As shown in Fig. 7b, the leveling torque is proportional to the tilt angle:

$$|\boldsymbol{\tau}_G| \sim \delta\left(\delta \to 0\right). \tag{20}$$

  However, as the tilt angle becomes larger ($\delta > 10°$), the leveling torque ceases to increase.
- $\boldsymbol{\tau}_G$ and h
  From Fig. 7(a), it can be observed that, under a fixed tilt angle, as the quadrotor's altitude gradually decreases, the leveling torque initially increases and then decreases, which is consistent with the trend observed in the simulation in Fig. 6. This validates our previous assumption in Sec. V-B1 and Sec. V-B2 and also calibrates the parameters of (18).

Conclusion 1:

As the height decreases, the absolute value of the leveling torque $|\tau_G|$ reaches a maximum at a certain distance from the ground, then gradually decreases, rather than monotonically increasing.

C. Mixing Matrix Model under Ground Effect

Ground effect has various impacts on the dynamic model of the quadrotor. We have reasons to suspect that the torque generated by rotor speed differences is also affected by ground effect, which means some parameters of the mixing control matrix in (4) (k_{TX}, k_{TY}, k_I) may vary with the state of the quadrotor. Therefore, we conduct experiments to validate this.

We fix the quadrotor onto the platform (Fig. 3(b)) and adjust the distance between the quadrotor and the ground board while ensuring the ground board is level. Then we drive the four rotors to rotate at varying speeds. Data on rotor speeds, heights and torques are collected.

The ground board is adjustable relative to the quadrotor's Y-axis, with a certain adjustment error that prevents the ground board from being perfectly level. The leveling torque still

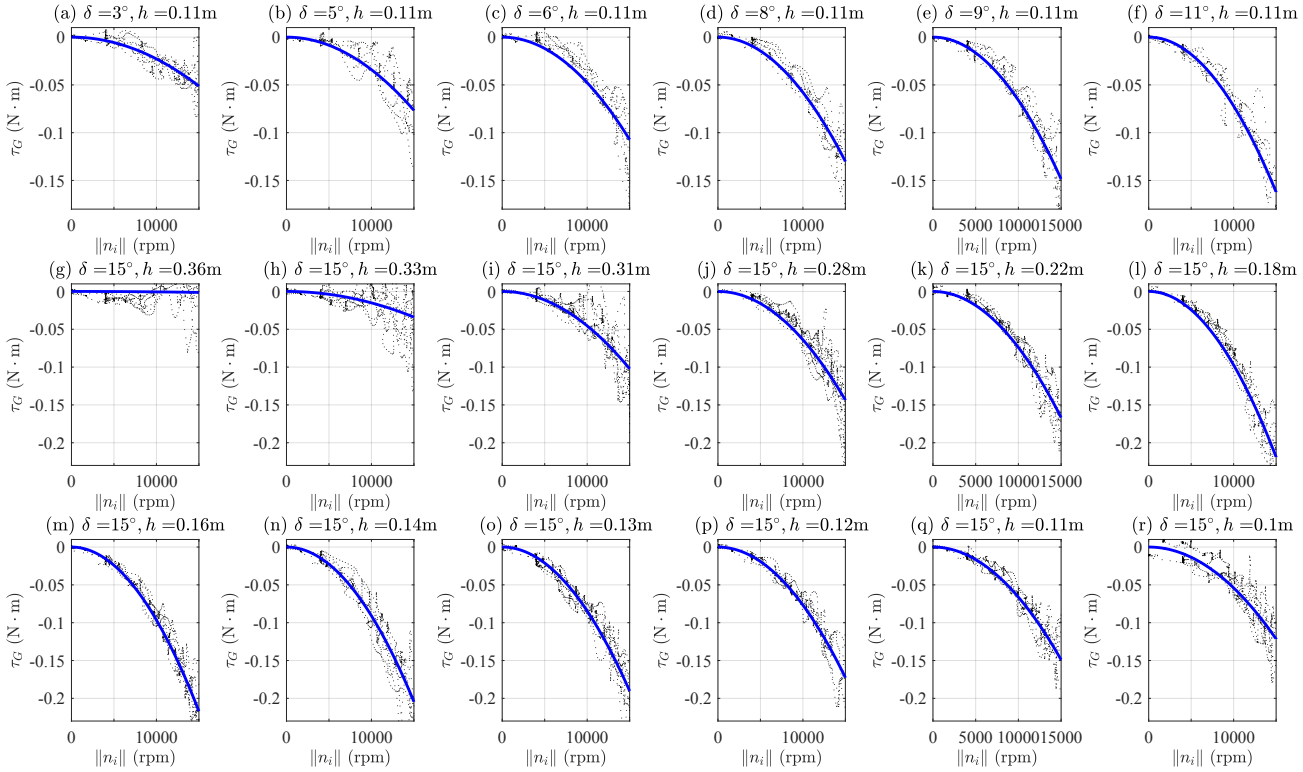

Fig. 8: Relationship between leveling torque $\boldsymbol{\tau}_G$ and average rotor speed $\|n_i\|$. The black points are sensor data and the blue lines are model-fitting results.

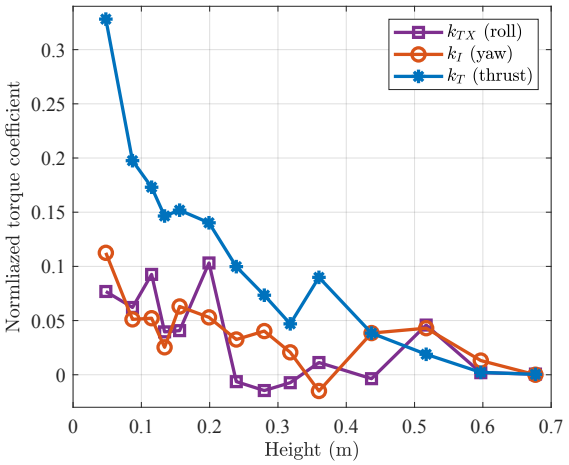

Fig. 9: The relationship between normalized torque coefficient and h.

exists on the Y-axis. Therefore, when studying the torque generated by thrust difference, we only focus on the X-axis and Z-axis (k_{TX}, k_I).

In TABLE. I, it can be seen that the body torque $\boldsymbol{\tau}_B$ is closely related to the rotor speed difference $\boldsymbol{N}_{base}$ and has no relationship with the altitude h. For example, $r_s\left[\boldsymbol{x}_W{}^\top \boldsymbol{\tau}_B, \boldsymbol{N}_{base}(2)\right] = 0.8400$, $r_s\left[\boldsymbol{x}_W{}^\top \boldsymbol{\tau}_B, h\right] = -0.0937$.

We calculate the relationship between each coefficient (k_T, k_{TX} and k_I) and the altitude respectively in Fig. 9. The coefficients in the figure are normalized with the following procedure:

$$\bar{k}(h) = \frac{k(h)}{k(+\infty)} - 1. \tag{21}$$

In Fig. 9, as the quadrotor descends from high altitude to the ground board, the change in torque coefficient (k_{TX} and k_I) generated by the rotor speed difference is negligible (less than 10%), compared to the change in thrust coefficient k_T (around 30%).

We believe this change is mainly caused by the mechanical vibrations near the ground, leading to measurement errors.

Conclusion 2:

The torque parameters of the mixing control matrix (k_{TX}, k_{TX}, k_I) remains *unaffected* by ground effect.

D. Rotor Drag under Ground Effect

When the multicopter is flying forward, a rotor drag opposite to the direction of motion is generated. It is proved that the drag is related to thrust and the flight speed along the horizontal direction of the multicopter's body system [21]:

$$\boldsymbol{f_D}(\boldsymbol{R}, \boldsymbol{v}, T) = -\boldsymbol{R}\boldsymbol{D}'\sqrt{T}\boldsymbol{R}^\top \boldsymbol{v}, \tag{22}$$

where $\boldsymbol{D}' = diag(d_x, d_y, 0)$ is the drag coefficient matrix.

Due to the inclusion of thrust T in this rotor drag term, the formulation of the rotor drag poses challenges for the derivation of the differential flatness of the multicopter dynamics.

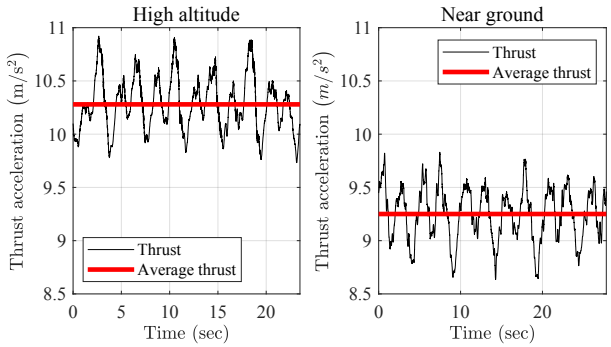

Fig. 10: Thrust differences during high altitude and near ground flight.

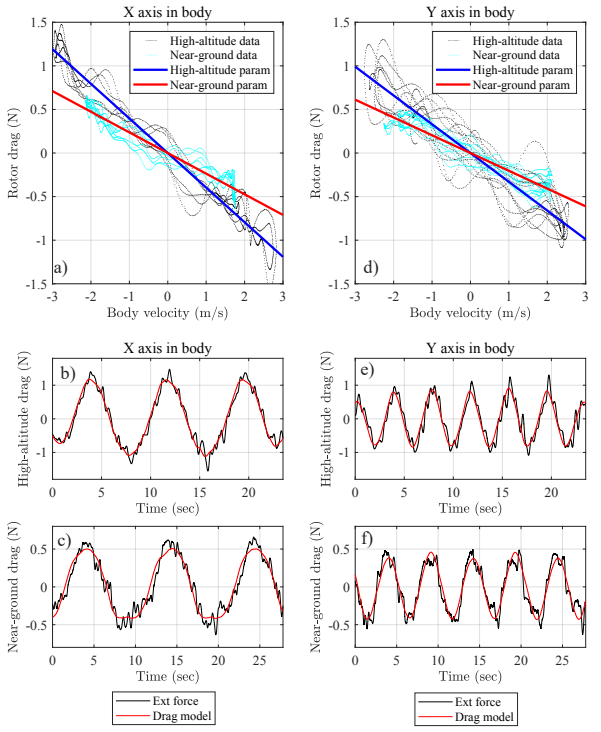

Fig. 11: Rotor drag at high altitude and near-ground conditions. (a)(d) the black and blue points represent data collected during quadrotor flights at high and low altitudes, respectively. The horizontal axis represents flight speed, and the vertical axis represents rotor drag in the body coordinate system.

Generally, when the multicopter is flying at a high altitude, the thrust is maintained near the hover throttle, which can be regarded as a fixed value [13]. When the quadrotor is flying near the ground, the hover thrust is reduced due to the extra thrust provided by $\boldsymbol{f}_G$, so the rotor drag will also decrease, in theory.

To verify the assumption, we conduct flight tests at both high and low altitudes. As shown in Fig. 10, the ratio of the average thrust at low and high altitude is:

$$\frac{\sqrt{T\left(0.1\right)}}{\sqrt{T\left(2.0\right)}}=0.9486, \tag{23}$$

which should also be the ratio of rotor drag at low and high altitudes according to (22). However, the experimental results in Fig. 11 show that:

$$\frac{d_x\left(0.1\right)}{d_x\left(2.0\right)}=0.5963, \frac{d_y\left(0.1\right)}{d_y\left(2.0\right)}=0.6179. \tag{24}$$

Conclusion 3:

The rotor drag f_D at low altitudes declines substantially beyond what current model(22) can predict.

The formation mechanism of this phenomenon cannot be explained theoretically at the moment. But in engineering, we can consider rotor drag as a function related to altitude and the specific curve can be measured experimentally and interpolated:

$$\boldsymbol{f}_D\left(\boldsymbol{R},\boldsymbol{v},h\right)=-\boldsymbol{R}\boldsymbol{D}\left(h\right)\boldsymbol{R}^{\top}\boldsymbol{v}. \tag{25}$$

VI. Differential Flatness with Ground Effect

In this section, we will explain that, even when considering the impact of ground effect, the quadcopter retains its differential flatness. By designating the quadcopter's position and yaw angle as its flat outputs, we can compute the quadcopter's thrust, attitude, angular velocity, angular acceleration, torque, and rotor speeds:

$$\begin{aligned}&\left\{\boldsymbol{p},\boldsymbol{v},\boldsymbol{a},\boldsymbol{j},\boldsymbol{s}\right\},\left\{\varphi,\dot{\varphi},\ddot{\varphi}\right\}\\ \leftrightarrow&T_{ref},\left\{\boldsymbol{\xi}_{ref},\boldsymbol{\omega}_{ref},\dot{\boldsymbol{\omega}}_{ref},\boldsymbol{\tau}_{Bref},\boldsymbol{n}_{ref}\right\}.\end{aligned} \tag{26}$$

The more types of disturbances we need to consider, the more complex the derivation process of differential flatness becomes. For example, when we only consider the rotor drag related to velocity [13], the multicopter needs to compensate for it by generating additional acceleration. However, the acceleration of a multirotor is coupled with its attitude, which means that the compensation for drag needs to be considered from acceleration to attitude and angular velocity reference outputs.

For multicopters affected by ground effects, the derivation process needs to consider models for additional thrust, altitude-varying rotor drag, and leveling torque.

Among these disturbances, the leveling torque, which is influenced by multiple factors, is the most complex. Although we calibrate the parameters in Sec. V-B, it only partially explains the model and is not entirely accurate. There are bound to be some differences between the situation with the torque measurement platform and real flight conditions. Therefore, we need to find a reasonable method to simplify or approximate the leveling torque model, ensuring it does not introduce distortion to the model while also not affecting the differential flatness of the multicopter.

A. The Payload Model Designed for Leveling Torque

The approach we take is to equate the leveling torque to the gravity torque generated by a Payload ball rigidly connected under the multicopter.

We enumerate **four** dynamic models which are **equivalent** to each other (refer to Fig. 13) during inner loop attitude control.

- **Payload, with external torque.**
  Euler's equation for a multicopter with a payload ball (Fig. 12) can be written as:

$$\begin{aligned}\boldsymbol{J}_1\dot{\boldsymbol{\omega}} = &-\boldsymbol{\omega}\times\boldsymbol{J}_1\boldsymbol{\omega}+\boldsymbol{\tau}_B \\ &+\boldsymbol{R}^\top\left(\boldsymbol{R}\begin{bmatrix}0\\0\\-\frac{m_0}{m}r\end{bmatrix}\times(-mg)\,\boldsymbol{z}_W\right).\end{aligned} \tag{27}$$

  Simplify it:

$$\boldsymbol{J}\dot{\boldsymbol{\omega}} = -\boldsymbol{\omega}\times\boldsymbol{J}\boldsymbol{\omega}+\boldsymbol{\tau}_B+m_0gr\boldsymbol{R}^\top(\boldsymbol{z}_B\times\boldsymbol{z}_W), \tag{28}$$

  where m is the mass of the multicopter, m_0 is the mass of the ball, r is the distance from the ball to the center of the multicopter.
- **Payload, without external torque.**
  In the model (28), if we move the control center of the multicopter from the gravity center of the itself down to the overall gravity center of the multicopter and the payload ball, then the Euler equation can be written as:

$$\boldsymbol{J}'\dot{\boldsymbol{\omega}} = -\boldsymbol{\omega}\times\boldsymbol{J}'\boldsymbol{\omega}+\boldsymbol{\tau}_B, \tag{29}$$

  where J' is the overall inertia moment at the new control center:

$$\boldsymbol{J}' = \boldsymbol{J}+diag\left\{\begin{array}{ccc} m\left(\frac{m_0}{m}r\right)^2 & m\left(\frac{m_0}{m}r\right)^2 & 0\end{array}\right\}. \tag{30}$$

- **Near ground, with leveling torque.**
  Euler's equation for a multicopter with leveling torque can be written as:

$$\boldsymbol{J}\dot{\boldsymbol{\omega}} = -\boldsymbol{\omega}\times\boldsymbol{J}\boldsymbol{\omega}+\boldsymbol{\tau}_B+M_G(h)\,T\boldsymbol{R}^\top(\boldsymbol{z}_B\times\boldsymbol{z}_W). \tag{31}$$

- **Near ground, without leveling torque.**
  The form of (31) and (28) will be the same if we set

$$m_0gr = M_G(h)\,T. \tag{32}$$

  Using the same method of moving the gravity center down, we can modify the leveling torque model (31) as:

$$\boldsymbol{J}'\dot{\boldsymbol{\omega}} = -\boldsymbol{\omega}\times\boldsymbol{J}'\boldsymbol{\omega}+\boldsymbol{\tau}_B. \tag{33}$$

  The adjusted inertia moment J' is

$$\boldsymbol{J}' = \boldsymbol{J}+diag\left\{\begin{array}{ccc}\frac{[M_G(h)T]^2}{mg^2} & \frac{[M_G(h)T]^2}{mg^2} & 0\end{array}\right\}. \tag{34}$$

Considering that the thrust is maintained around the hover throttle, it can be assumed:

$$M_G(h)\,T\approx\frac{mgM_G(h)}{1+F_G(h)}. \tag{35}$$

Combined with (34) and (35), the modified inertia moment $\boldsymbol{J}'(h)$ is only related to the height from the ground (Fig. 13).

In general, the change of inertia moment can be handled by adjusting the PID parameters or the LQR method [29], [30] . In order to deal with other unknown disturbances, we propose a method that combining model-based and model-free disturbance resistance, which will be introduced in detail in Sec. VII.

B. Thrust and Attitude Outputs

The model with additional thrust, altitude-varying rotor drag and inertia moment can be written as:

$$\begin{aligned}&\boldsymbol{a} = -g\boldsymbol{z}_W+[1+F_G(h)]\,T_a\boldsymbol{z}_B-\boldsymbol{R}\boldsymbol{D}_a(h)\,\boldsymbol{R}^\top\boldsymbol{v}\\ &\boldsymbol{J}(h)\,\dot{\boldsymbol{\omega}} = -\boldsymbol{\omega}\times\boldsymbol{J}(h)\,\boldsymbol{\omega}+\boldsymbol{\tau}_B,\end{aligned} \tag{36}$$

where $T_a = T/m$ and $\boldsymbol{D}_a(h) = \boldsymbol{D}(h)/m$ are the normalized accelerations.

Left multiply $\boldsymbol{z}_b$ to the following formula:

$$\begin{aligned}\boldsymbol{a}+g\boldsymbol{z}_W+\left[d_{ax}(h)\,\boldsymbol{x}_B{}^\top\boldsymbol{v}\right]\boldsymbol{x}_{\boldsymbol{B}}+\left[d_{ay}(h)\,\boldsymbol{y}_B{}^\top\boldsymbol{v}\right]\boldsymbol{y}_B\\ -[1+F_G(h)]\,T_a\boldsymbol{z}_B = 0.\end{aligned} \tag{37}$$

The reference thrust can be obtained:

$$T = m\frac{\boldsymbol{z}_B{}^\top(\boldsymbol{a}+g\boldsymbol{z}_W)}{[1+F_G(h)]}. \tag{38}$$

Left multiply $\boldsymbol{x}_b$ and $\boldsymbol{y}_b$ to (37), we can get the reference attitude:

$$\begin{aligned}&\boldsymbol{x}_B{}^\top\boldsymbol{\alpha} = 0, \boldsymbol{\alpha}{=}\boldsymbol{a}+g\boldsymbol{z}_{\boldsymbol{W}}+d_x(h)\,\boldsymbol{v}\\ &\boldsymbol{y}_B{}^\top\boldsymbol{\beta} = 0, \boldsymbol{\beta}{=}\boldsymbol{a}+g\boldsymbol{z}_{\boldsymbol{W}}+d_y(h)\,\boldsymbol{v}\\ &\boldsymbol{x}_B = \frac{\boldsymbol{y}_C\times\boldsymbol{\alpha}}{\|\boldsymbol{y}_C\times\boldsymbol{\alpha}\|}, \boldsymbol{y}_B = \frac{\boldsymbol{\beta}\times\boldsymbol{x}_B}{\|\boldsymbol{\beta}\times\boldsymbol{x}_B\|}, \boldsymbol{z}_B = \boldsymbol{x}_B\times\boldsymbol{y}_B.\end{aligned} \tag{39}$$

An intermediate reference frame is defined as:

$$\begin{bmatrix}\boldsymbol{x}_C & \boldsymbol{y}_C & \boldsymbol{z}_C\end{bmatrix} = T_Z(\varphi)\left(\begin{bmatrix}\boldsymbol{x}_W & \boldsymbol{y}_W & \boldsymbol{z}_W\end{bmatrix}\right). \tag{40}$$

C. Other Outputs

We can obtain the reference outputs of angular velocity $\boldsymbol{\omega}_{ref}$ and angular acceleration $\dot{\boldsymbol{\omega}}_{ref}$ by differentiating the acceleration in (36) The detailed derivation process is similar to [13]. In the differentiation process, since the multicopter generally does not have a significant Z-axis velocity when executing a near-ground flight trajectory, we can assume that $\frac{d}{dt}D(h) = \frac{d^2}{dt^2}D(h) = 0$.

Then the reference torque input can be obtained:

$$\boldsymbol{\tau}_{ref} = \boldsymbol{J}'(h)\,\dot{\boldsymbol{\omega}}_{ref}+\boldsymbol{\omega}_{ref}\times\boldsymbol{J}'(h)\,\boldsymbol{\omega}_{ref}. \tag{41}$$

VII. Model-based Controller with Incremental Inversion

This section will use the previously introduced model to compensate for external disturbances, thereby controlling the quadrotor during near-ground flight. The most important part is the compensation of the leveling torque in Sec. VII-C.

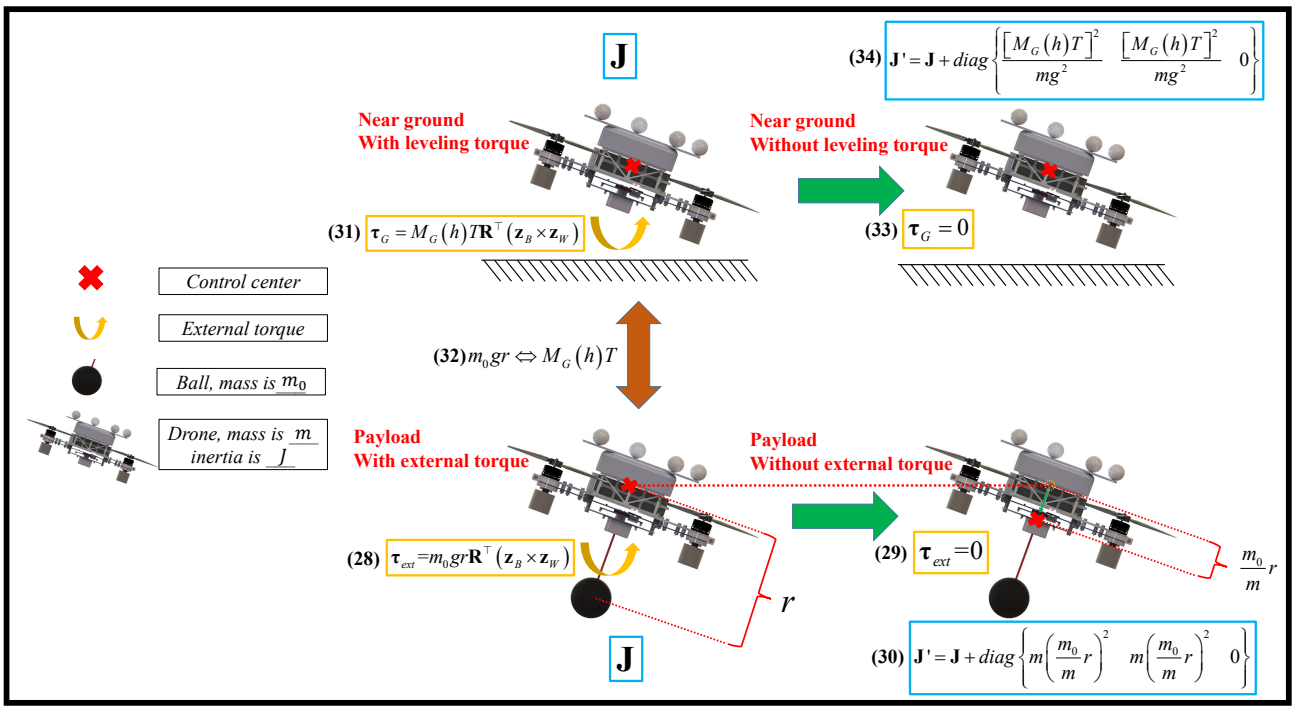

Fig. 12: The multicopter affected by the leveling torque is equivalent to a multicopter with a payload below. The dynamic models of the four cases in the figure can be mutually equivalent. Ultimately, the influence of leveling torque can be equivalent to changes in the inertia moment of the multicopter. The specific explanation is provided in Sec. VI-A

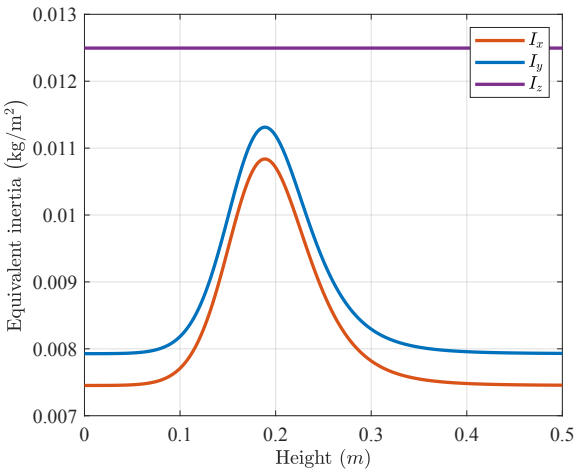

Fig. 13: Equivalent inertia moment of the quadrotor in the counterweight ball model.

A. Acceleration Command

Generally, there are two ways to compensate for external forces acting on the multicopter.

- Using an external force observer to introduce the resultant external acceleration into the control loop, which is called the *dynamic inversion*, This approach does not rely on the accurate model but may suffer from delays and noises of the external force estimation.
- Predicting the external forces at the desired state use them as feedforward compensation, which needs accurate calibrated dynamic model.

Given that we establishe an accurate external force model, we rely on the thrust and drag models to compensate to avoid noise and control errors.

The expected resultant acceleration is

$$\boldsymbol{a}_{des} = \boldsymbol{a}_{ref} + \boldsymbol{a}_E - \boldsymbol{a}_D - \boldsymbol{a}_G. \tag{42}$$

$\boldsymbol{a}_{ref}$ represents the reference acceleration (26) along the motion trajectory.

$\boldsymbol{a}_E$ is the acceleration resulting from the position and velocity error feedback:

$$\boldsymbol{a}_E = \boldsymbol{K}^P \left(\boldsymbol{p}_{des} - \hat{\boldsymbol{p}}\right) + \boldsymbol{K}^V \left(\boldsymbol{v}_{des} - \hat{\boldsymbol{v}}\right), \tag{43}$$

where $\boldsymbol{K}^P$ and $\boldsymbol{K}^V$ are the parameters of the Proportional-Differential (PD) controller for position control.

$\boldsymbol{a}_D$ is the acceleration obtained from the drag model (25):

$$\boldsymbol{a}_D = -\boldsymbol{R}\frac{\boldsymbol{D}(h)}{m}\boldsymbol{R}^\top \boldsymbol{v}_{ref}. \tag{44}$$

$\boldsymbol{a}_G$ is the acceleration obtained from the additional thrust model (10):

$$\boldsymbol{a}_G = \frac{T_{ref}}{m} F_G(h)\, \boldsymbol{z}_B. \tag{45}$$

B. Attitude, Bodyrate and Body Acceleration Command

We can get the desired attitude from the desired acceleration using the principles of differential flatness in Sec. VI:

$$\boldsymbol{a}_{des} \leftrightarrow \boldsymbol{\xi}_{des}. \tag{46}$$

The error between the current attitude $\hat{\boldsymbol{\xi}}$ and the expected attitude $\boldsymbol{\xi}_{des}$ is:

$$\boldsymbol{\xi}_e = \hat{\boldsymbol{\xi}} \circ \boldsymbol{\xi}_{des}. \tag{47}$$

The attitudes here are all quaternion forms. The $\circ$ means the Hamilton quaternion product.

Write it into an angle vector:

$$\boldsymbol{\xi}_e{}' = \frac{2\cos^{-1}\boldsymbol{\xi}_e^w}{\sqrt{1-\boldsymbol{\xi}_e^{w\,2}}}\begin{bmatrix} \boldsymbol{\xi}_e^x & \boldsymbol{\xi}_e^y & \boldsymbol{\xi}_e^z \end{bmatrix}^\top, \tag{48}$$

where $\begin{bmatrix} \boldsymbol{\xi}^w & \boldsymbol{\xi}^x & \boldsymbol{\xi}^y & \boldsymbol{\xi}^z \end{bmatrix}$ is the quaternion form of the attitude.

Subsequently, we can calculate the desired angular velocity and angular acceleration:

$$\begin{aligned} \boldsymbol{\omega}_{des} &= \boldsymbol{K}^{\boldsymbol{\xi}}\boldsymbol{\xi}_e{}' + \boldsymbol{\omega}_{ref} \\ \dot{\boldsymbol{\omega}}_{des} &= \boldsymbol{K}^{\omega}\left(\boldsymbol{\omega}_{des} - \boldsymbol{\omega}_f\right) + \dot{\boldsymbol{\omega}}_{ref}. \end{aligned} \tag{49}$$

In this context, $\boldsymbol{K}^{\boldsymbol{\xi}}$ and $\boldsymbol{K}^{\omega}$ are the PD parameters for angle control, and $\boldsymbol{\omega}_{ref}$, $\dot{\boldsymbol{\omega}}_{ref}$ are the reference angular velocity and angular acceleration derived from (26) respectively.

C. Thrust and Torque Command

The desired acceleration projected onto the quadrotor's Z-axis corresponds to the acceleration the rotors need to produce. Then we can get the expected thrust:

$$T_{des} = m\boldsymbol{a}_{des}\frac{\hat{\boldsymbol{z}}_B}{|\hat{\boldsymbol{z}}_B|}. \tag{50}$$

The torque required from the motors can be calculated based on the desired angular velocity and desired angular acceleration:

$${}^B\boldsymbol{\tau}_{des} = \boldsymbol{J}'\left(h\right)\cdot\dot{\boldsymbol{\omega}}_{des} + \boldsymbol{\omega}_{des}\times\boldsymbol{J}'\left(h\right)\cdot\boldsymbol{\omega}_{des}. \tag{51}$$

The rotational inertia $\boldsymbol{J}'\left(h\right)$, which is altitude-dependent, serves to compensate for the torque effects induced by ground effect.

Due to various reasons, the above method cannot completely compensate for the external torques. Firstly, the parameters obtained based on the torque measurement platform are not entirely accurate. Secondly, there are other unmodeled torques, such as the gravity torque and the gyroscopic torque. Therefore, we combine the incremental nonlinear dynamic inversion [20] with our model to output the control torque:

$${}^B\boldsymbol{\tau}_{des} = \hat{\boldsymbol{\tau}}_B + \boldsymbol{J}'\left(h\right)\cdot\left(\dot{\boldsymbol{\omega}}_{des} - \dot{\boldsymbol{\omega}}_f\right). \tag{52}$$

There are two explanations for the altitude-varying of inertia moment $\boldsymbol{J}'\left(h\right)$ in the control method:

- The leveling torque change rapidly. If we directly apply the traditional INDI method, the compensation for the torque is not strong enough:

$$\left|\boldsymbol{J}\cdot\left(\dot{\boldsymbol{\omega}}_{des} - \dot{\boldsymbol{\omega}}_f\right)\right| < \left|\boldsymbol{J}'\left(h\right)\cdot\left(\dot{\boldsymbol{\omega}}_{des} - \dot{\boldsymbol{\omega}}_f\right)\right|. \tag{53}$$

- Compensation for the external torque by real-time estimation essentially introduces feedback for angular acceleration error $\left(\dot{\boldsymbol{\omega}}_{des} - \dot{\boldsymbol{\omega}}_f\right)$, where the gain is the fixed inertia moment of $\boldsymbol{J}$. If $\boldsymbol{J}$ is adjustable, it means that the angular acceleration error gain is flexible and can adapt to changes in flight conditions.

In practice, we still need to fine-tune the function $\boldsymbol{J}'\left(h\right)$ during the experiment. The model-based compensation method then degrades to adjust the gain of the angular acceleration error. This gives our approach an engineering value as well as a scientific explanation: parameters can be adjusted based on actual flight conditions, rather than having to rely on a parameter calibration platform strictly.

D. Rotor Speed Command

Based on the inverse of the mixed control matrix in (4), the rotational speeds of each motor can be computed from the thrust and torques:

$$\boldsymbol{N}_{des}{}^2 = M^{-1}\begin{bmatrix} T_{des} \\ {}^B\boldsymbol{\tau}_{des} \end{bmatrix}. \tag{54}$$

E. Calibration for Rotors

To control the rotors to the desired speeds, the rotors need to be modeled and calibrated.

1) Thrust and Torque Generated by a Single rotor: The thrust (T_i) and torque (M_i) generated by a single rotor [31], [32] are

$$\begin{aligned} T_i &= k_T {n_i}^2 \\ M_i &= k_I n^2 + J_R\dot{n}_i, \end{aligned} \tag{55}$$

where k_T is the thrust coefficient, k_I is the torque coefficient, J_R is the moment of inertia of the rotor and i is the rotor number.

The parameters in (55) are calibrated on the single-rotor platform in Fig. 3(a). Fig. 14 shows the actual and predicted thrust and torque generated by the rotor.

2) Throttle of the ESC: When the flight controller receives a throttle control signal ($t_c \in [0,1]$), the rotor speed will be maintained at a roughly determined value. The relationship between the rotor speed and the throttle, after eliminating the influence of battery voltage, is usually a quadratic function:

$$n_{esc}\left(t_c\right) = c_2{t_c}^2 + c_1 t_c + c_0. \tag{56}$$

We refine the code of the APM [1] firmware to align with the throttle interface and voltage compensation logic, which will be open-sourced in the future.

We collect rotor speed and throttle data on the single-motor platform and calibrate the model. The data is illustrated in Fig. 15.

[1]https://github.com/ArduPilot/ardupilot

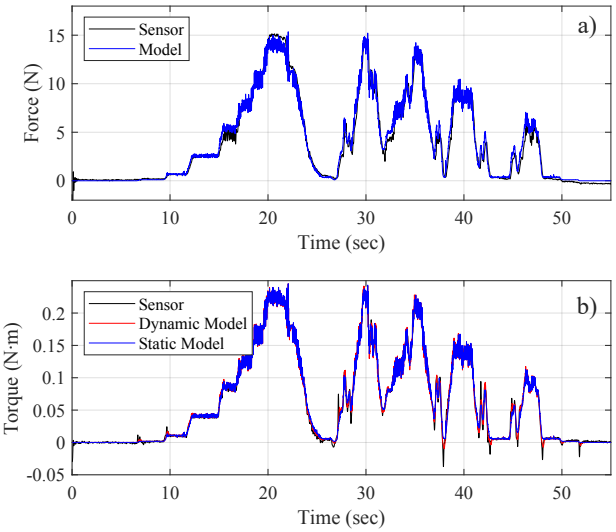

Fig. 14: Calibration of the (a)thrust and (b)torque model of a single rotor. Static/dynamic model: without/with a differential term of rotor speed $\dot{n}$.

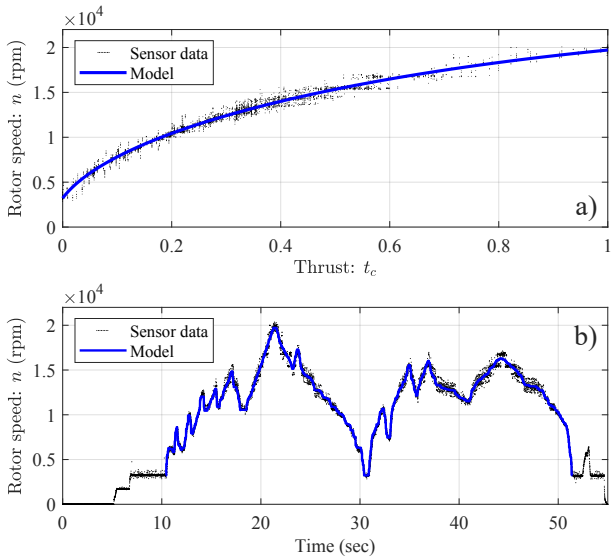

Fig. 15: Throttle Curve Calibration. (a) The relationship between rotor speed n and throttle t_c. (b) Time series of motor speed, with the blue line representing the speed predicted using the throttle model (56).

F. Throttle Command

The rotor speeds are controlled through the throttle input ($t_i^{des} \in [0, 1]$), and the rotational speeds are fed back through *BDhot*. The rotor speeds require closed-loop control, but we do not implement it for each motor individually. Instead, we implement closed-loop control on the combined acceleration generated by all rotors along $\boldsymbol{z}_B$. Our experimental results indicate that this approach leads to a more stable multicopter attitude. The control method for rotor speed is:

$$\begin{aligned} t_i^{des} &= t_i^{ref} + t_E \\ t_i^{ref} &= n_{esc}^{-1}(n_i) \\ t_E &= K_P^T T_a^E + K_I^T \sum T_a^E \\ T_a^E &= \left(\sum_{i=1}^{4} k_T {n_i^{des}}^2 - \sum_{i=1}^{4} k_T {n_i}^2 \right) / m, \end{aligned} \tag{57}$$

where t_i^{ref} is the feedforward throttle obtained by n_{esc}^{-1}, the inverse function of (56), t_E is the throttle from rotor speed error, T_a^E is the acceleration error by all rotors, K_P^T, K_I^T are the parameters of the Proportional-Integral controller.

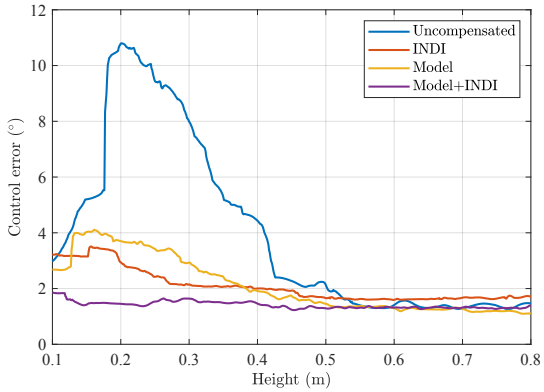

Fig. 16: Hovering angle error with different control methods.

VIII. Flight Experiment

We set up a quadrotor flight platform for comparison experiments. The quadrotor has a larger blade diameter ($r = 7$inch) and a smaller propeller distance to the ground ($h_{\min} = 7.2$cm). These factors make the ground effect of the quadrotor more obvious. The controller in Sec. VII is compared with other control methods through hovering and trajectory tracking experiments.

The quadrotor is equipped with a flight controller [2] that can feedback 200Hz IMU data. The flight controller using an APM firmware version that supports *BDhot* can communicate bidirectionally with the motor controller and read the rotor speed data at 200Hz. A 16×16 lattice laser sensor [3] is mounted under the quadrotor to measure the distance to the ground (at 100Hz). An Intel NUC [4] is used as the computing platform. A label holder for the NOKOV [5] motion capture system is fixed to the top of the computer. The motion capture system and IMU are fused through Extended Kalman Filter (EKF) [33], [34], and a smooth location result (200Hz) is obtained.

[2]https://doc.cuav.net/flight-controller/v5-autopilot/en/v5+.html
[3]https://www.nooploop.com/tofsense-m/
[4]https://www.intel.com/content/www/us/en/products/sku/205603/intel-nuc-11-pro-kit-nuc11tnki5/specifications.html
[5]https://en.nokov.com/products/motion-capture-cameras/Mars.html

TABLE III: Comparison of controllers.

Experiment	Acceleration Compensation	Torque Compensation	Height	Velocity	RMSE (cm) XOY	RMSE (cm) Z	RMSE (cm) All	$\max\left(\|\boldsymbol{E}_P\|_2\right)$ (cm)	$\sigma\left(\|\boldsymbol{E}_P\|_2\right)$ (cm)
1	-	-	0.12m	1m/s	6.54	8.64	10.85	18.04	2.19
2	INDI	-	0.12m	1m/s	**5.51**	6.83	8.77	**16.07**	**2.06**
3	Neural Land	-	0.12m	1m/s	6.81	4.94	8.41	16.75	2.73
4	Proposed	-	0.12m	1m/s	7.12	**1.94**	**7.38**	16.45	3.05
5	Proposed	Proposed	0.12m	1m/s	**4.35**	**0.97**	**4.45**	**11.97**	2.32
6	Proposed	-	0.18m	3m/s	12.63	**1.71**	12.74	26.27	5.36
7	Proposed	Proposed	0.18m	3m/s	**6.67**	2.84	**6.97**	**14.66**	**2.72**
8	Proposed	Proposed	1.75m	5m/s	**4.77**	**1.41**	**4.98**	**9.75**	**1.64**

A. Hovering Experiment

We hover the quadrotor from high to low altitude and compare the angle control errors. The error value at a specific altitude is defined as:

$$E\left(h_0\right)=\left\|\hat{\boldsymbol{\xi}}-\boldsymbol{\xi}_{des}\right\|_2\left(h\in\left[h_0-\Delta h,h_0+\Delta h\right]\right). \quad (58)$$

Fig. 16 shows how the control error varies with altitude. When no compensation is applied, the angle error at low altitude is huge, reaching its peak at $h=0.2m$. This corresponds to the model in Sec. V-B, where the leveling torque in Fig.7 reaches its maximum at $h=0.18m$.

Both the model-based method in (51) and INDI [20] can effectively reduce the control error, but the angle error near the ground is still increased compared with the high altitude. When the combined model and incremental inverse method (52) is used, the error at low altitude is the same as that at high altitude.

B. Trajectory Tracking Experiment

We generate lemniscate trajectories [35] for tracking experiments in TABLE. III.

Executing the trajectory at $v=1m/s$ without torque compensation, we conduct four sets of experiments to compare our acceleration compensation method with INDI [20], neural landing [17], and the no-compensation method [13].

INDI performs only slightly better than no compensation in the Z-axis. This could be because INDI compensates for the acceleration of external forces with real-time estimation. However, a slight error in compensation for the external force in the Z-axis can affect the multicopter's altitude, and the altitude change will further affect the external force in the Z-axis, which leads to a static control error.

The reasonable approach is to compensate with the predicted external force under the desired state, as seen in the proposed method. The proposed method performs the best in the Z-axis, which is expected, as the feedforward curve of $\boldsymbol{f}_G$ is finely calibrated based on the multicopter.

In these four sets of experiments, INDI has the best control performance in the XOY plane. This might be because the attitude cannot track the acceleration perfectly due to the external torques, but INDI can introduce acceleration into the feedback loop for compensation.

With the torque compensation, the proposed method achieves the best control accuracy at $1m/s$ and $3m/s$ trajectories. Fig. 17 shows the curves of the $3m/s$ trajectory. Every loop is well-controlled, including the rotor speed, thrust acceleration, body torque, etc.

To assess the controller's extreme performance, we conduct a trajectory test at a high altitude of $5\mathrm{m/s}$. Our controller achieves an RMSE of $4.98\mathrm{cm}$. The controller does perform well, but low-altitude flight still hurts trajectory tracking.

IX. Discussion and Future Work

This paper summarizes various models of the multicopter under ground effect and establishes a control methodology. We consider the additional thrust, leveling torque, and rotor drag models under ground effect and validate its impact on the mixing matrix. However, our study has several limitations. Firstly, we do not model the thrust decrease during high-speed forward flight [15]. This is mainly due to two reasons: our models are primarily calibrated at static force platforms, and our flight speed does not reach the threshold that would produce a significant loss of lift. In our flight scenarios, the flight speed remains below the induced speed of $4m/s$, and the minimum flight altitude is larger than the propeller radius, resulting in the lift reduction being not obvious and, therefore, not considered. However, Exp.6 and Exp.7 in TABLE. III indicate that high-speed flight impacts the control effectiveness along the Z-axis. Secondly, our study on the decrease of rotor drag is not thorough enough. The causes of rotor drag involve complex airflow phenomena [12], and the ground effect further complicates the situation. We hope that future research will explain this phenomenon clearly.

We will open source the simulation environment, various mechanical model and dataset after publication.

References

[1] J. Fishman, S. Ubellacker, N. Hughes, and L. Carlone, "Dynamic grasping with a" soft" drone: From theory to practice," in *2021 IEEE/RSJ International Conference on Intelligent Robots and Systems (IROS)*, 2021, pp. 4214–4221.

[2] J. Saunders, S. Saeedi, and W. Li, "Autonomous aerial robotics for package delivery: A technical review," *Journal of Field Robotics*, vol. 41, no. 1, pp. 3–49, 2024.

[3] S. Gao, C. Di Franco, D. Carter, D. Quinn, and N. Bezzo, "Exploiting ground and ceiling effects on autonomous uav motion planning," in *2019 IEEE International Conference on Unmanned Aircraft Systems (ICUAS)*, 2019, pp. 768–777.

[4] L. Wang, H. Xu, Y. Zhang, and S. Shen, "Neither fast nor slow: How to fly through narrow tunnels," *IEEE Robotics and Automation Letters*, vol. 7, no. 2, pp. 5489–5496, 2022.

[5] R. Ding, Y.-H. Hsiao, H. Jia, S. Bai, and P. Chirarattananon, "Passive wall tracking for a rotorcraft with tilted and ducted propellers using proximity effects," *IEEE Robotics and Automation Letters*, vol. 7, no. 2, pp. 1581–1588, 2022.

[6] C. Luo, X. Li, Y. Li, and Q. Dai, "Biomimetic design for unmanned aerial vehicle safe landing in hazardous terrain," *IEEE/ASME Transactions on Mechatronics*, vol. 21, no. 1, pp. 531–541, 2015.

[7] J. Ji, T. Yang, C. Xu, and F. Gao, "Real-time trajectory planning for aerial perching," in *2022 IEEE/RSJ International Conference on Intelligent Robots and Systems (IROS)*, 2022, pp. 10 516–10 522.

[8] C. Powers, D. Mellinger, A. Kushleyev, B. Kothmann, and V. Kumar, "Influence of aerodynamics and proximity effects in quadrotor flight," in *Experimental Robotics: The 13th International Symposium on Experimental Robotics*. Springer, 2013, pp. 289–302.

[9] P. Sanchez-Cuevas, G. Heredia, and A. Ollero, "Characterization of the aerodynamic ground effect and its influence in multirotor control," *International Journal of Aerospace Engineering*, vol. 2017, 2017.

[10] X. He, G. Kou, M. Calaf, and K. K. Leang, "In-ground-effect modeling and nonlinear-disturbance observer for multirotor unmanned aerial vehicle control," *Journal of Dynamic Systems, Measurement, and Control*, vol. 141, no. 7, 2019.

[11] P. Wei, S. N. Chan, S. Lee, and Z. Kong, "Mitigating ground effect on mini quadcopters with model reference adaptive control," *International Journal of Intelligent Robotics and Applications*, vol. 3, no. 3, pp. 283–297, 2019.

[12] P.-J. Bristeau, P. Martin, E. Salaün, and N. Petit, "The role of propeller aerodynamics in the model of a quadrotor uav," in *2009 IEEE European control conference (ECC)*, 2009, pp. 683–688.

[13] M. Faessler, A. Franchi, and D. Scaramuzza, "Differential flatness of quadrotor dynamics subject to rotor drag for accurate tracking of high-speed trajectories," *IEEE Robotics and Automation Letters*, vol. 3, no. 2, pp. 620–626, 2017.

[14] J. Svacha, K. Mohta, and V. Kumar, "Improving quadrotor trajectory tracking by compensating for aerodynamic effects," in *2017 international conference on unmanned aircraft systems (ICUAS)*. IEEE, 2017, pp. 860–866.

[15] X. Kan, J. Thomas, H. Teng, H. G. Tanner, V. Kumar, and K. Karydis, "Analysis of ground effect for small-scale uavs in forward flight," *IEEE Robotics and Automation Letters*, vol. 4, no. 4, pp. 3860–3867, 2019.

[16] I. Cheeseman and W. Bennett, "The effect of the ground on a helicopter rotor in forward flight," 1955.

[17] G. Shi, X. Shi, M. O'Connell, R. Yu, K. Azizzadenesheli, A. Anandkumar, Y. Yue, and S.-J. Chung, "Neural lander: Stable drone landing control using learned dynamics," in *2019 IEEE International Conference on Robotics and Automation (ICRA)*, 2019, pp. 9784–9790.

[18] X. He, M. Calaf, and K. K. Leang, "Modeling and adaptive nonlinear disturbance observer for closed-loop control of in-ground-effects on multi-rotor uavs," in *Dynamic Systems and Control Conference*, vol. 58295. American Society of Mechanical Engineers, 2017, p. V003T39A004.

[19] H. Du, Z. Pu, J. Yi, and H. Qian, "Advanced quadrotor takeoff control based on incremental nonlinear dynamic inversion and integral extended state observer," in *2016 IEEE Chinese Guidance, Navigation and Control Conference (CGNCC)*, 2016, pp. 1881–1886.

[20] E. Tal and S. Karaman, "Accurate tracking of aggressive quadrotor trajectories using incremental nonlinear dynamic inversion and differential flatness," *IEEE Transactions on Control Systems Technology*, vol. 29, no. 3, pp. 1203–1218, 2020.

[21] J. M. Kai, G. Allibert, M. Hua, and T. Hamel, "Nonlinear feedback control of quadrotors exploiting first-order drag effects," *Ifac Papersonline*, vol. 50, no. 1, pp. 8189–8195, 2017.

[22] M. de Carvalho and F. J. Marques, "Jackknife euclidean likelihood-based inference for spearman's rho," *North American Actuarial Journal*, vol. 16, no. 4, pp. 487–492, 2012.

[23] K. Christodoulou, M. Vozinidis, A. Karanatsios, E. Karipidis, F. Katsanevakis, and Z. Vlahostergios, "Aerodynamic analysis of a quadcopter drone propeller with the use of computational fluid dynamics." *CET Journal-Chemical Engineering Transactions*, vol. 76, 2019.

[24] Y. M. Park and S. Jee, "Numerical study on interactional aerodynamics of a quadcopter in hover with overset mesh in openfoam," *Physics of Fluids*, vol. 35, no. 8, 2023.

[25] S. Weerasinghe and M. Monasor, "Simulation and experimental analysis of hovering and flight of a quadrotor," 2017.

[26] A. Thai, R. Jain, and S. Grace, "Cfd validation of small quadrotor performance using createtm-av helios," in *VFS 75th Annual Forum & Technology Display*, 2019.

[27] S. S. Shamsudin and M. Z. Madzni, "Aerodynamic analysis of quadrotor uav propeller using computational fluid dynamic," *Journal of Complex Flow*, vol. 3, no. 2, pp. 28–32, 2021.

[28] Q. Guo, Y. Zhu, Y. Tang, C. Hou, Y. He, J. Zhuang, Y. Zheng, and S. Luo, "Cfd simulation and experimental verification of the spatial and temporal distributions of the downwash airflow of a quad-rotor agricultural uav in hover," *Computers and Electronics in Agriculture*, vol. 172, p. 105343, 2020.

[29] M. Faessler, D. Falanga, and D. Scaramuzza, "Thrust mixing, saturation, and body-rate control for accurate aggressive quadrotor flight," *IEEE Robotics and Automation Letters*, vol. 2, no. 2, pp. 476–482, 2016.

[30] D. Falanga, K. Kleber, S. Mintchev, D. Floreano, and D. Scaramuzza, "The foldable drone: A morphing quadrotor that can squeeze and fly," *IEEE Robotics and Automation Letters*, vol. 4, no. 2, pp. 209–216, 2018.

[31] J. Brandt and M. Selig, "Propeller performance data at low reynolds numbers," in *49th AIAA Aerospace Sciences Meeting including the New Horizons Forum and Aerospace Exposition*, 2011, p. 1255.

[32] K. Zhang, T. Yang, Z. Ding, S. Yang, T. Ma, M. Li, C. Xu, and F. Gao, "The visual-inertial-dynamical multirotor dataset," in *2022 IEEE International Conference on Robotics and Automation (ICRA)*, 2022, pp. 7635–7641.

[33] V. Madyastha, V. Ravindra, S. Mallikarjunan, and A. Goyal, "Extended kalman filter vs. error state kalman filter for aircraft attitude estimation," in *AIAA Guidance, Navigation, and Control Conference*, 2011, p. 6615.

[34] J. Sola, "Quaternion kinematics for the error-state kalman filter," *arXiv preprint arXiv:1711.02508*, 2017.

[35] Z. Wang, X. Zhou, C. Xu, and F. Gao, "Geometrically constrained trajectory optimization for multicopters," *IEEE Transactions on Robotics*, vol. 38, no. 5, pp. 3259–3278, 2022.

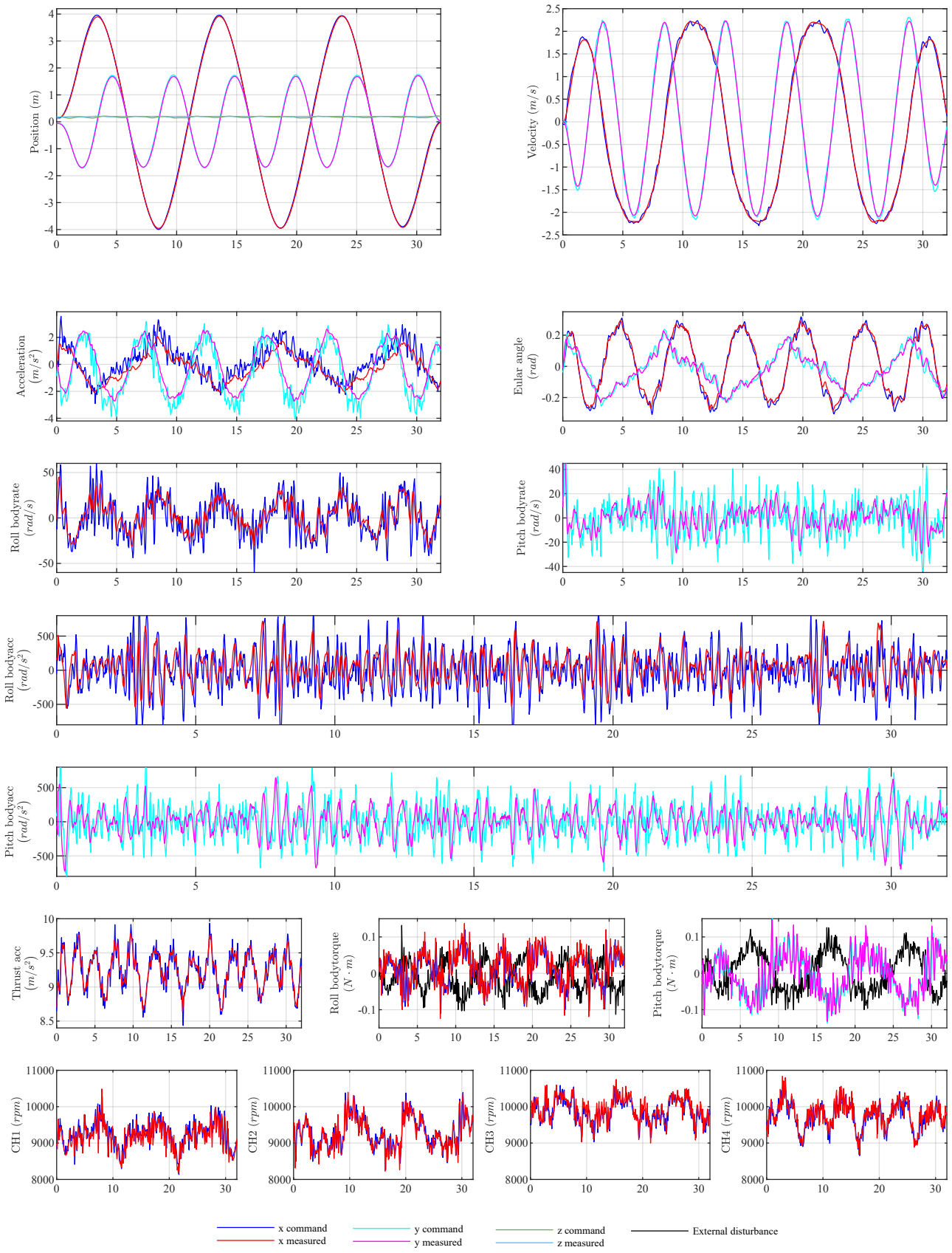

Fig. 17: Tracking curve of each control object in the near ground flight test (3m/s).